Japanese Journal of Applied Physics **53**, 07KF09 (2014) **REGULAR PAPER**
http://dx.doi.org/10.7567/JJAP.53.07KF09

Optimization of feature extraction for automated identification of heart wall regions in different cross sections

Kohei Nakahara[1], Hideyuki Hasegawa[1,2], and Hiroshi Kanai[1,2*]

[1]*Graduate School of Engineering, Tohoku University, Sendai 980-8579, Japan*
[2]*Graduate School of Biomedical Engineering, Tohoku University, Sendai 980-8579, Japan*
E-mail: kanai@ecei.tohoku.ac.jp

Received November 29, 2013; accepted March 5, 2014; published online June 13, 2014

In most current methods of evaluating the cardiac function based on echocardiography, the heart wall in an ultrasonic image is currently identified manually by an operator. However, this task is very time-consuming and leads to inter- and intraobserver variability. To facilitate the analysis and eliminate operator dependence, automated identification of heart wall regions is essential. We previously proposed a method of automatic identification of heart wall regions using multiple features based on information of the amplitude and phase of the ultrasonic RF echo signal by pattern recognition. In the present study, we investigate a new method of segmenting an ultrasonic image into the heart wall, lumen, and external tissues (includes pericardium) by two-step pattern recognition. Also, parameters in the proposed classification method were examined for application to different cross sections, i.e., long-axis and short-axis views, by considering differences in the motion and echogenicity of the heart walls. Furthermore, moving target indicator (MTI) filtering to suppress echoes from clutters was improved to enhance the separability in the short-axis view. © 2014 The Japan Society of Applied Physics

1. Introduction

Echocardiography is an indispensable modality for the diagnosis of cardiac diseases because it is noninvasive, cost effective, and easy to use. Also, the echocardiographic methods for the early detection of cardiac diseases (e.g., myocardial ischemia), have been developed.[1)] In conventional echocardiography, the structural change and macroscopic motion of the heart are diagnosed by measuring cross-sectional images, and, owing to the high temporal resolution, quantitative evaluation of intracardiac blood flow and cardiac wall motion can also be done by ultrasound Doppler measurements.[1,2)] Furthermore, various valuable methods for evaluating the cardiac function on the basis of echocardiography have been developed, such as the evaluation of two-dimensional (2D) cardiac wall motion and strain rate by the speckle tracking method,[3–7)] measurement of the propagation of vibration caused by the closure of heart valves,[8)] and strain rate imaging at high spatial and high temporal resolution, which measures the transient of myocardial contraction and relaxation for about 10 ms.[9,10)] In addition, it was reported that the myocardial strain rate, estimated from the temporal change of the integrated backscatter signal, which is obtained by averaging the ultrasonic scattering power from a region of interest in myocardial tissue, reflects the contractile and relaxant characteristics fairly well.[11)]

In most of the above-mentioned methods, the heart wall (myocardium), which is the object to be analyzed, is currently identified manually by an operator on a cross-sectional image of the heart. However, this task is very tedious and time-consuming, and it causes inter- and intraobserver variability.[12–14)] To eliminate operator dependence and facilitate analysis, automated identification of the heart wall is demanded.

Various studies on segmenting regions in ultrasonic images have been conducted. Ibrahim et al. proposed techniques for the detection of arterial wall boundaries for assessing the intima-media thickness of the carotid arterial wall.[15,16)] Chang et al. classified the thyroid gland and directly estimated its volume in ultrasonic images.[17)] In the cited studies, objects in an ultrasonic image are segmented using features extracted from the magnitude of the received ultrasonic signal. Furthermore, Torp et al. proposed a method for automatic detection of several candidate points in the apical view of the left ventricle.[18)] This method also yields features from the gray-scale value (intensity of an ultrasound image), the velocity, and the depth of each image point to detect the candidate points.

On the other hand, a method has been reported for the identification of an object of interest, i.e., heart wall or lumen, on an echocardiographic image by pattern recognition using the information of the ultrasonic echo signal. Nillesen et al. introduced a method in which echogenicity was smoothed in each local area to suppress speckle noise in the lumen.[19)] However, the method using only echogenicity would misclassify a region with low echogenicity inside the heart wall as lumen. To overcome this limitation, Kinugawa et al. proposed a method of identifying the heart wall using the magnitude-squared coherence (MSC) function, which evaluates the variance of the phase shift of the RF signal among consecutive frames,[20)] and it shows a greater separability of the heart wall and lumen. Takahashi et al. further improved the segmentation by using multiple features including echogenicity and magnitude-squared coherence.[21,22)] The separabilities of multiple features change depending on the behavior of the heart and, thus, the optimal cardiac phase for feature extraction was determined by quantitative evaluation of the separability. As a result, a more accurate segmentation in a frame in the optimal cardiac phase was achieved. The heart wall region in each frame throughout an entire cardiac cycle can be identified by tracking the points in the heart wall region identified by proposed pattern recognition in a certain frame using a tracking method.

However, the above-mentioned method can be applied to only the ultrasonic data obtained in the long-axis view of the heart [Fig. 1(a)]. The echogenicity of the lateral wall of the left ventricle in the short-axis view [Fig. 1(b)] is low owing to the small angle between the ultrasonic beam and the direction of the myocardial fiber.[23)] In addition, the MSC of the heart wall is low owing to the movement of the heart wall in the direction perpendicular to the ultrasonic beam.

 © 2014 The Japan Society of Applied Physics

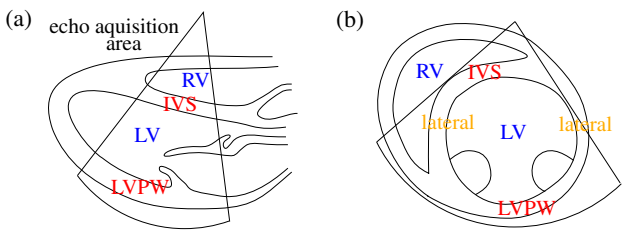

Fig. 1. (Color online) Illustrations of measurement by transthoracic echocardiography in (a) long-axis view and short-axis view of left ventricle (RV: right ventricle, LV: left ventricle, IVS: interventricular septum, LVPW: left ventricular posterior wall).

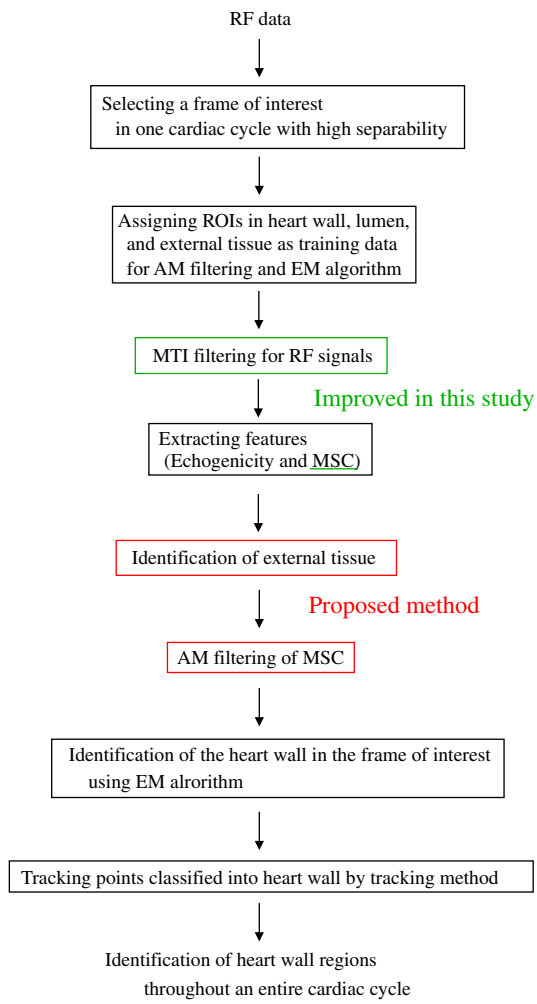

Fig. 2. (Color online) Schematic diagram of procedure of identification of the heart wall proposed in the present study.

Therefore, the classification in the short-axis view is difficult. In the present study, the extraction of features from ultrasonic echoes was optimized also for measurement in the short-axis view. Furthermore, the optimum cardiac phase was examined by evaluating the separability of the extracted features.

2. Principles

2.1 Feature extraction

Figure 2 shows the procedure proposed in the present study for automated identification of the heart wall in ultrasound data throughout an entire cardiac cycle. At the beginning, the frame of interest (FOI) is selected from the optimal cardiac phase[21] for classification. Then, the ultrasonic data in the FOI is classified into the heart wall, lumen, and external tissue by two-step pattern recognition. To perform pattern recognition, small regions of interest (ROIs) were manually assigned in the heart wall, lumen, and external tissue in the FOI, as shown in Fig. 3(a), to obtain training data. After the classification in the FOI, the heart wall regions in each frame in an echocardiographic image sequence during one cardiac cycle is identified by tracking the points in the heart wall region identified in the FOI by 2D tracking methods. In the step of pattern recognition, the information of the amplitude and phase of the ultrasonic RF echo signal is used. The first feature is echogenicity, which is equivalent to information of the amplitude of the ultrasonic RF signal. The magnitude-squared coherence (MSC) function, which evaluates the temporal variance in the phase shifts in ultrasonic echoes, can be used to improve the separability.[20] Using the extracted multiple features, the heart wall regions in the FOI are identified by automatically determining the threshold between features of the classes (heart wall and lumen regions) using the expectation-maximization (EM) algorithm.[24]

In this method, features, which were extracted with respect to all points of received RF signals, were calculated from signals in each spatial window in the axial direction, with a size of 1.44 mm (= 28 points) corresponding to the length of an ultrasonic pulse. Similar to conventional segmentation of echocardiographic images, the echogenicity was used as the first feature in the present study. The echogenicity $G_n(i, j)$ of a discrete point at the j-th sampled point in the axial direction in the i-th beam and the n-th frame was extracted from the received ultrasonic RF echo signal $s(i, j)$ as follows:

$$G_n(i, j) = \log_{10}[\mathrm{LPF}_j[(s_n(i, j))^2]], \tag{1}$$

where $\mathrm{LPF}_j[\cdot]$ denotes low-pass filtering in the direction of depth with a cut-off frequency of 0.3 MHz (nominal transmit ultrasonic center frequency: 3.75 MHz).

The heart wall is not completely distinguished from the lumen using only the echogenicity because there are regions with low echo levels inside the heart wall. Hete and Shung found that the magnitude of the ultrasonic backscattered signals were changed depending on the orientation of muscle collagen fibers.[25] Wickline et al. suggested that the magnitude of ultrasonic backscatter is determined by local differences in acoustic impedance, which are affected by myocardial contraction and relaxation.[26] Thus, an additional second feature, i.e., the MSC function, was adopted in our method. The MSC is defined as follows:

$$|\gamma_n(i, j; f)|^2 = \frac{\left|\sum_{k=0}^{N-1} Y^*_{n+k}(i, j + \widehat{m}(n+k); f) Y_{n+k+1}(i, j + \widehat{m}(n+k+1); f)\right|^2}{\sum_{k=0}^{N-1} |Y_{n+k}(i, j + \widehat{m}(n+k); f)|^2 \sum_{k=0}^{N-1} |Y_{n+k+1}(i, j + \widehat{m}(n+k+1); f)|^2}, \tag{2}$$

© 2014 The Japan Society of Applied Physics

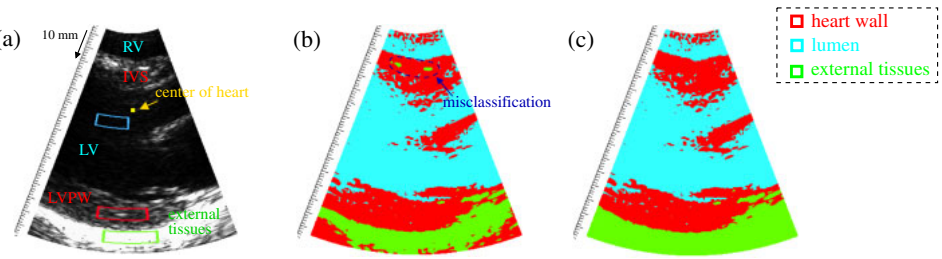

Fig. 3. (Color online) Result of identification of external tissue: (a) B-mode image with gravity center estimated using echo amplitude and manually assigned areas for heart wall, lumen, and external tissue. (b) Region-identified image. (c) Region-identified image corrected using distance from gravity center.

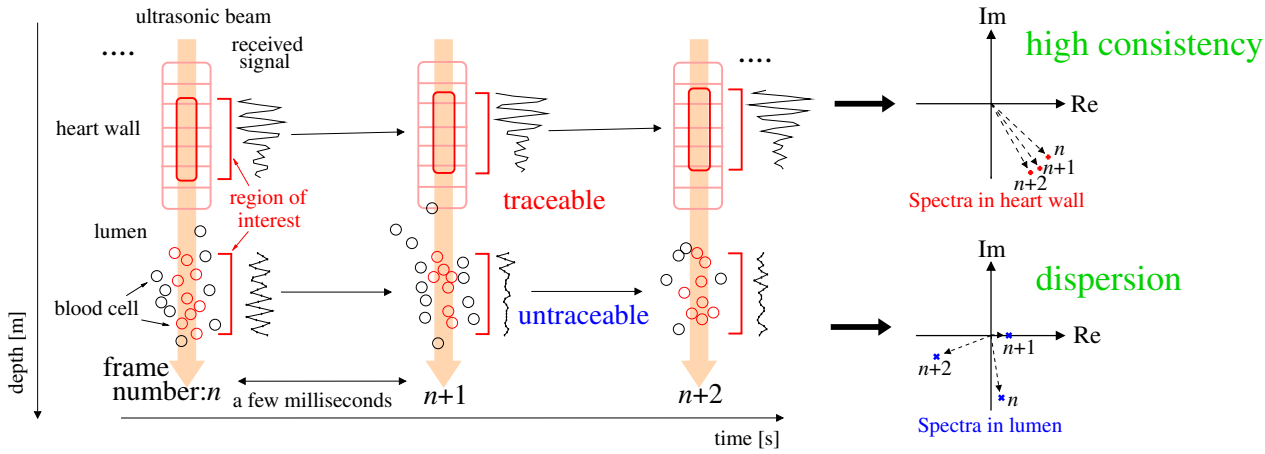

Fig. 4. (Color online) Illustration of changes in waveforms of echo signals in ROI.

where * and N denote a complex conjugate and the number of frames used for estimating the MSC, respectively, and $\widehat{m}(n)$ corresponds to the displacement of the point of interest (i, j) in the n-th frame estimated by the *phased-tracking method*.[27] The details of the estimation of the MSC is described in references,[20,28] and the frequency f was set at 4.82 MHz. As illustrated in Fig. 4, the temporal changes in waveforms of RF echo signals in an ROI placed in the heart wall region are fairly small and can be tracked. Therefore, the MSC in the heart wall becomes high. On the other hand, blood cells in the cardiac lumen are difficult to track because they are moving fast owing to blood flow and slip off the ultrasonic beam. Therefore, the temporal change in the waveform of an ultrasonic echo in an ROI assigned in the lumen is significant. Therefore, the MSC becomes high in the heart wall region and low in the lumen region. However, the MSC of RF signals, the second feature, is also increased because of the components of echoes from stationary or slowly moving clutter, such as the ribs.[20] In addition, there is a considerable difference between the acoustic impedances of clutter and blood particles. Therefore, the echogenicity and MSC become higher when echoes from clutters are included. Thus, reduction of the clutter component is necessary to accurately extract the features, particularly from the cardiac lumen. In the present study, in order to reduce echoes from clutters, a high-pass filter with respect to the frame[29] was used as a moving target indicator (MTI) filter[30] for RF signals before calculating the first and second features, $G_n(i, j)$ and $|\gamma_n(i, j)|^2$.[21,22] There are clutter echoes particularly in shallow regions, e.g., clutter echoes from ribs, and, thus, the clutter echoes dominantly influence the echoes from a shallow region in the heart, e.g., the right ventricle. Therefore, in the present study, MTI filtering was applied to the region with depth limited to 33 mm to suppress reduction of the necessary signal, i.e., echoes from the heart wall and lumen.

2.2 Improvement of estimated MSC distribution by adaptive mean filtering

In the present study, adaptive mean (AM) filtering, which smooths spatial features, is applied to reduce the undesired spatial fluctuation in the estimated MSC distribution and improve the separability of the second feature, i.e., MSC. The AM filtering is expressed as follows:

$$\hat{c} = \mu + k(c - \mu), \tag{3}$$

$$k = \frac{\sigma - \sigma_{\min}}{\sigma_{\max} - \sigma_{\min}}, \tag{4}$$

$$k = \begin{cases} 0 & \text{if } k < 0 \\ 1 & \text{if } k > 1 \end{cases}, \tag{5}$$

where μ and σ are the mean and standard deviation of MSC in each $6 \times 6\,\mathrm{mm}^2$ (in horizontal and vertical directions) region (window) containing 30×30 data points (center of the window is the point of interest). The original ultrasonic RF data were obtained in a sector format and, thus, the original ultrasonic data were interpolated so that 30×30 data points were included in each $6 \times 6\,\mathrm{mm}^2$ window. In this interpolation, the value (MSC) of the nearest original sampled

© 2014 The Japan Society of Applied Physics

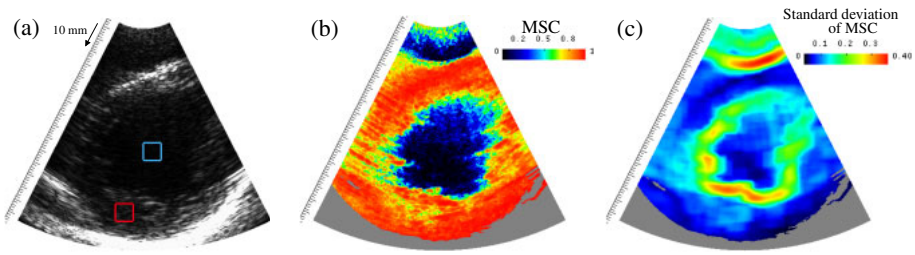

Fig. 5. (Color online) Example of MSC image of short-axis view of left ventricle: (a) B-mode image. (b) MSC image. (c) Standard deviation of MSC in each local region.

point was used as the value of each interpolated point. Figures 5(a)–5(c) show examples of a B-mode image, MSC image unprocessed by AM filtering, and standard deviation of MSC in each local region (window), respectively. In the present study, the standard deviation obtained with respect to the manually assigned ROI for the heart wall [region surrounded with red line in Fig. 5(a)] was used as the lower limit of standard deviation $\sigma_{\min}$ (corresponding to the case when there is no boundary in a window for AM filtering). On the other hand, the standard deviation obtained from the data (MSC) included in both the manually assigned ROIs for the heart wall and lumen was used as the upper limit of standard deviation $\sigma_{\max}$ (corresponding to the case when there is a boundary between the heart wall and lumen in a window). Using the original MSC c at the point of interest and a variable coefficient k, which was determined from estimated standard deviations, the filtered MSC $\hat{c}$ was obtained. The AM filter outputs the mean in a $6 \times 6\,\mathrm{mm}^2$ window to smooth the MSC distribution when the standard deviation σ is low (there is no boundary). On the other hand, the smoothing effect of the AM filter is suppressed when the standard deviation σ is high (there is a boundary). Using the AM filter, the separability is considered to be improved by information of surrounding points even when there is a peculiar point, e.g., low MSC in the heart wall owing to a low signal-to-noise ratio of an echo signal.

2.3 First-step classification: Identification of external tissue

In the present study, we proposed a method by two-step pattern recognition for classification of an ultrasonic image into three regions, i.e., heart wall, lumen, and external tissue. In the first step, external tissue is identified and excluded from the second step for segmentation of the heart wall and lumen. In the first pattern recognition, the ultrasonic data was classified into the heart wall, lumen, and external tissue by the EM algorithm using only the echogenicity. Figure 3(b) is an example of the result of classification based on the echogenicity. In Fig. 3(b), there are small regions misclassified as external tissue in the interventricular septum (IVS), which must be corrected. This misclassification was corrected using the geometrical information of each point. To obtain the geometrical information, the gravity center $c(c_i, c_j)$ [yellow dot in Fig. 3(a)] was obtained as a rough position near the center of the left ventricle as follows:

$$D(i,j) = 1 - \frac{G(i,j)}{G_{\max}}, \tag{6}$$

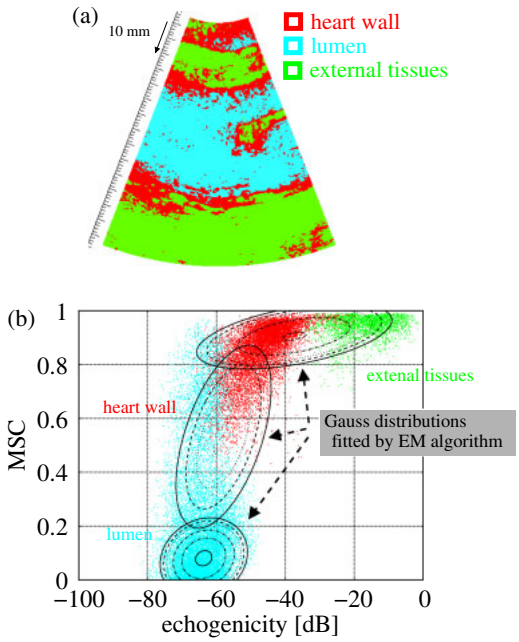

Fig. 6. (Color online) (a) Result of classification of heart wall, lumen, and external tissue by one-step classification using EM algorithm.
(b) Distributions of feature vectors of region manually assigned as each tissue and Gaussian distributions fitted by EM algorithm.

$$c_i = \frac{\sum_i \sum_j i \cdot D(i,j)}{\sum_i \sum_j D(i,j)}, \tag{7}$$

$$c_j = \frac{\sum_i \sum_j j \cdot D(i,j)}{\sum_i \sum_j D(i,j)}, \tag{8}$$

where $G_{\max}$ is the maximum of echogenicity in the entire ultrasonic data and $D(i, j)$ corresponds to the darkness of the point of interest (i, j) in the B-mode image. The echogenicity in the lumen is, in general, low, and the position of the lumen can be estimated roughly using the gravity center $c(c_i, c_j)$ obtained by weights of darkness $D(i, j)$.

The distance between the gravity center $c(c_i, c_j)$ and each point classified as the heart wall based on echogenicity was averaged to obtain the mean distance from the gravity center $c(c_i, c_j)$ to the heart wall. Using this mean distance, a point, which was classified as external tissue and whose distance from the gravity center $c(c_i, c_j)$ is shorter than the mean distance from the gravity center $c(c_i, c_j)$ to the heart wall, was corrected as the heart wall.

The advantage of two-step pattern recognition is described below. Figure 6(a) shows the result obtained by single-step

© 2014 The Japan Society of Applied Physics

classification into the heart wall, lumen, and external tissue using the EM algorithm with two features (i.e., echogenicity and MSC). Misclassification of the heart wall as external tissue is frequently observed. Figure 6(b) shows the feature distributions in the regions manually assigned as the heart wall, lumen, and external tissue and the estimated Gaussian distributions fitted to features of the respective regions. The reason for misclassification of the heart wall as external tissue is that the Gaussian distribution finally determined by the EM algorithm does not appropriately fit the measured features, as shown in Fig. 6(b), particularly for the heart wall. The separability of MSC to distinguish the heart wall (red points) from external tissue (green points) is low because the MSCs of the heart wall and external tissue are similar (high MSCs). Therefore, most of the data in the heart wall and external tissue can be explained by the Gaussian distribution obtained for external tissue, as can be seen in Fig. 6(b), and the data that cannot be explained by the Gaussian distributions obtained for the lumen and external tissue are explained by the Gaussian distribution obtained for the heart wall. Such a failure of estimation of the probability density function (Gaussian distribution) leads to significant classification errors in Fig. 6(a). Therefore, the data from external tissue, which have MSCs similar to those in the heart wall, should be removed before applying the EM algorithm for the classification of the heart wall and lumen.

2.4 Second-step classification: identification of heart wall and lumen

In this method, the data points classified as external tissue in the first classification were excluded in the second classification. The other data points were classified into the heart wall and lumen using two features, i.e., echogenicity and MSC, using the EM algorithm.[21] In the measured RF dataset of each cross section (long-axis and short-axis views), the regions of the heart wall and lumen were manually assigned as training data for classification based on the EM algorithm.[24] Using the EM algorithm, a mixture of two Gaussian distributions (corresponding to the heart wall and lumen) was fitted to features of the data points, and the line where the probabilities of the determined Gaussian distributions were the same was used as the threshold for the classification of each data point. Using the 2D feature vector $\boldsymbol{d}_{i,j} = (G(i,j), |\gamma(i,j)|^2)$ extracted at each discrete point (i, j) in an acquisition area, the mixing coefficient $\{\pi_h\}$, mean vectors $\{\boldsymbol{\mu}_h\}$, and covariance matrices $\{\boldsymbol{\Sigma}_h\}$ were obtained for classes $\{\omega_h\}$ [lumen ($h = 0$) and heart wall ($h = 1$)] as follows:

$$\pi_h = \frac{N_h}{N} \quad (h \in \{0, 1\}), \tag{9}$$

$$\boldsymbol{\mu}_h = \mathrm{E}_{i,j}[\boldsymbol{d}_{i,j}|\omega_h] \quad (h \in \{0, 1\}), \tag{10}$$

$$\boldsymbol{\Sigma}_h = \mathrm{E}_{i,j}[(\boldsymbol{d}_{i,j} - \boldsymbol{\mu}_h)(\boldsymbol{d}_{i,j} - \boldsymbol{\mu}_h)^{\mathrm{T}}|\omega_h] \quad (h \in \{0, 1\}), \tag{11}$$

where $\mathrm{E}_{i,j}[\cdot]$ denotes spatial averaging in the axial and the lateral directions, and N_h, N, and $\boldsymbol{\mu}_h$ are the number of feature vectors belonging to each class, the total number of vectors in the area for evaluation, and the mean vector in each class, respectively.

In the first iteration, the measured ultrasonic data were classified using covariance matrices $\{\boldsymbol{\Sigma}_h\}$, mean vectors $\{\boldsymbol{\mu}_h\}$ and mixing coefficient $\{\pi_h\}$ obtained from the manually assigned training data. In the subsequent iterations, covariance matrix $\boldsymbol{\Sigma}_h$, mean vector $\boldsymbol{\mu}_h$ and mixing coefficient π_h were updated from feature vectors $\{\boldsymbol{d}_{i,j}\}$ classified into the corresponding class using the previous covariance matrix, mean vector and π_h. The iteration maximizes the likelihood of a mixture of Gaussian distributions, which represents the degree of fitting, and the iteration was stopped when the likelihood converged to a local maximum value.

3. Experimental results and discussion

3.1 Determination of optimal cardiac phase and number of frames for calculation of MSC

We previously reported that the optimal cardiac phase for classification of the heart wall in the long-axis view is the period from the rapid-filling phase to the slow-filling phase.[21] In the present study, the optimal cardiac phase for the short-axis view was also determined. In addition, the number of frames N for the calculation of MSC, which is the important parameter for determining the separability of MSC, was examined. A larger number of frames is desirable for statistically stable estimation of MSC. However, an excessive number of frames degrades the separability of MSC because tracking errors are more likely to occur. Therefore, the optimum cardiac phase and number of frames should be examined for each cross section, i.e., long-axis and short-axis views.

Ultrasonic RF echoes were acquired from the long-axis and short-axis views of the heart of a healthy 25-year-old male, using a 3.75 MHz phased array probe. By parallel beamforming (PBF)[31,32] with plane wave transmission, high-frame-rate (long-axis: 860 Hz, short-axis: 560 Hz) measurements of RF echoes were realized with 0.375° intervals of scan lines. The sampling frequency of the measured RF signals was 15 MHz.

To evaluate the separability of the feature vector, the interclass covariance matrix $\boldsymbol{S}_B$ in Eq. (14), which corresponds to the distance between mean vectors of classes (heart wall and lumen), and the intraclass covariance matrix $\boldsymbol{S}_W$ in Eq. (15), which corresponds to the mean variances of feature vectors within classes, were defined using these parameters as follows:

$$p_h = \frac{N_h}{N} \quad (h \in \{0, 1\}), \tag{12}$$

$$\boldsymbol{\mu} = \sum_{h=0}^{1} p_h \mathrm{E}_{i,j}[\boldsymbol{d}_{i,j}|\omega_h], \tag{13}$$

$$\boldsymbol{S}_B = \sum_{h=0}^{1} p_h(\boldsymbol{\mu}_h - \boldsymbol{\mu})(\boldsymbol{\mu}_h - \boldsymbol{\mu})^{\mathrm{T}}, \tag{14}$$

$$\boldsymbol{S}_W = \sum_{h=0}^{1} p_h \boldsymbol{\Sigma}_h. \tag{15}$$

Separability of the feature vector increases in proportion to the distance between mean vectors of classes, whereas it decreases in proportion to the variances of vectors within classes.[24] Therefore, the criterion of separability J is defined by normalizing the interclass covariance matrix $\boldsymbol{S}_B$ by the intraclass covariance matrix $\boldsymbol{S}_W$ as follows:[33]

$$J = \mathrm{tr}[\boldsymbol{S}_W^{-1}\boldsymbol{S}_B], \tag{16}$$

where $\mathrm{tr}[\cdot]$ represents the sum of diagonal components.

© 2014 The Japan Society of Applied Physics

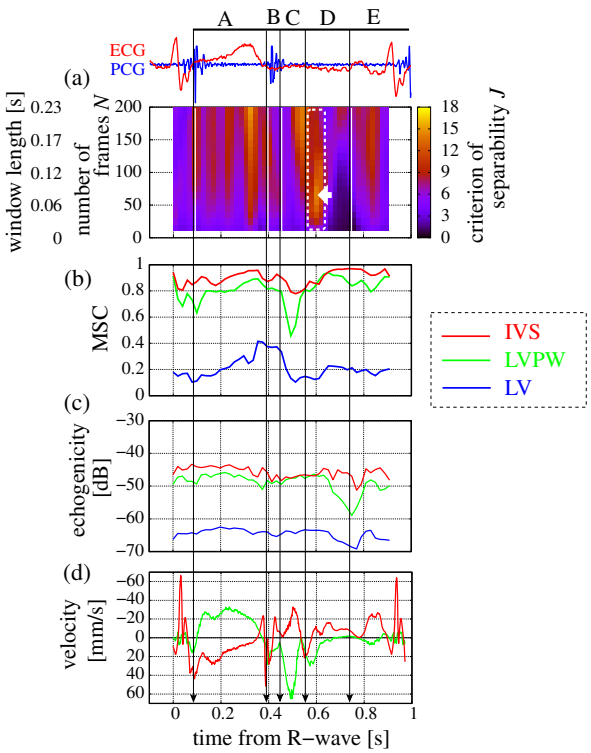

Fig. 7. (Color online) Results obtained in long-axis view of left ventricle: (a) Criterion of separability J. Spatial means of (b) MSC, (c) echogenicity, and (d) velocities.

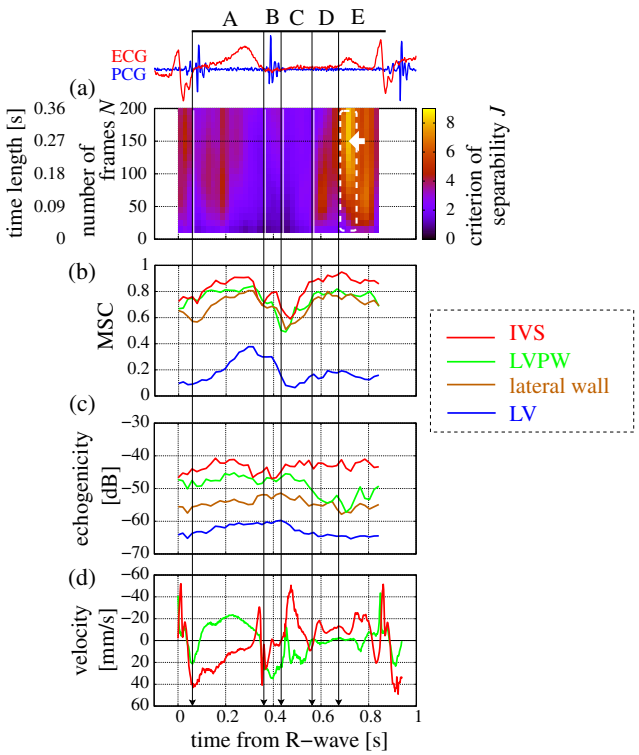

Fig. 8. (Color online) Results obtained in short-axis view of left ventricle: (a) Criterion of separability J. Spatial means of (b) MSC, (c) echogenicity and (d) velocities.

Figures 7(a) and 8(a) show the estimated separabilities in the long-axis and short-axis views of the left ventricle with different numbers of frames N for the calculation of MSC. Periods A, B, C, D, and E denote the ejection phase, isovolumic relaxation phase, rapid-filling phase, slow-filling phase, and atrial systole, as indicated in Figs. 7 and 8. The white lines in Figs. 7(a) and 8(a) indicate the optimal cardiac phases. The white arrows in Figs. 7(a) and 8(a) show the time and the number of frames, which give the maximal value of J. As shown in Fig. 7(a), the maximal value of J is found in the early slow-filling phase D when N is 70. The optimal cardiac phase agreed with that reported by Takahashi et al., and the reason is the large difference in MSCs between the heart wall and lumen, as shown in Fig. 7(b).[21]

On the other hand, as shown in Fig. 8(a), the maximal value of J is found in the atrial systole when N is 150. Figure 9 shows mean MSCs in the respective regions in the short-axis view with different numbers $\{N\}$ of frames in the early slow filling phase D (shown by the solid lines) and early atrial systole (shown by the dashed lines). As shown in Fig. 9, MSC of the lateral wall in the slow filling phase becomes markedly lower as the number of frames N increases. The motion velocity of the wall estimated by the *phased-tracking method* in the slow-filling phase is higher than that in the atrial systole, as shown in Fig. 8(d). Therefore, the separability in the slow-filling phase is lower than that in the atrial systole because the MSC of the lateral wall becomes lower mainly as a result of the fast movement of the heart wall in the direction perpendicular to the ultrasonic beam. As a result, the optimal cardiac phase for the short-axis view is the early atrial systole when the movement of the heart wall is slower than that in the slow-filling phase.

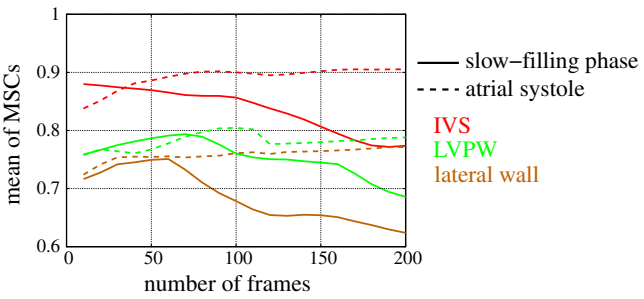

Fig. 9. (Color online) Mean of MSCs of short-axis view data in rapid filling phase and atrial systole.

The motion velocities of IVS and LVPW are evaluated in the atrial systole because the *phased-tracking method* cannot estimate the velocity of the lateral wall in the direction perpendicular to the ultrasonic beam.

Furthermore, the optimal number of frames N for the calculation of MSC was determined for each cross section. The number of frames N showing a high separability for the long-axis view was 40–100 frames corresponding to 0.05–0.12 s [= 0.074/(heart rate)] in the early slow-filling phase and 177 frames corresponding to 0.21 s [= 0.187/(heart rate)] in the early atrial systole. For the short-axis view, the optimal number of frames N showing high separability was 50–70 frames corresponding to 0.09–0.13 s [= 0.09/(heart rate)] in the slow-filling phase and 130–150 frames corresponding to 0.23–0.27 s [= 0.21/(heart rate)] in the atrial systole. Two ultrasonic datasets from the long-axis and short-axis views were acquired under different conditions, e.g., different frame rates and heart rates. Therefore, the

© 2014 The Japan Society of Applied Physics

Table I. Summary of optimal cardiac phase and number of frames N in each cross section.

Cross section in left ventricle	Optimal cardiac phase	Optimal number of frames N
Long-axis view	Early slow filling phase	70 frame [= 0.08 s, 0.074/(heart rate)]
Short-axis view	Early atrial systole	150 frame [= 0.27 s, 0.22/(heart rate)]

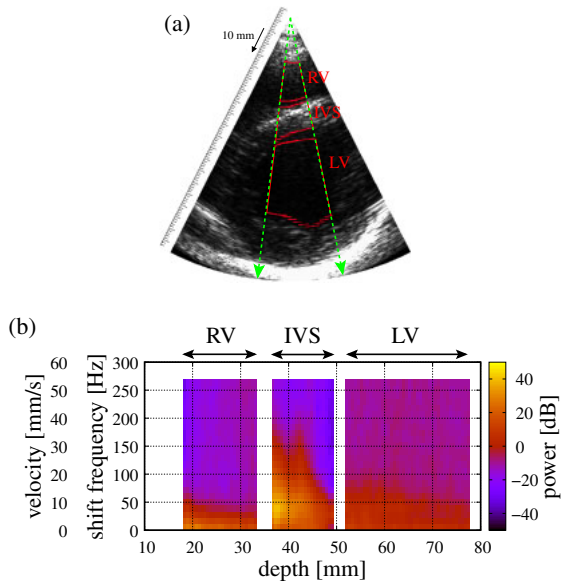

Fig. 10. (Color online) (a) Regions manually assigned for evaluation of power spectra of RF echoes (RV: right ventricle, LV: left ventricle, IVS: interventricular septum). (b) Power spectra at each depth obtained by averaging spectra in all beams in the assigned regions.

optimal number of frames N was expressed by the percentage to a cardiac cycle. The optimal number of frames N in the slow filling phase was smaller than that in the atrial systole in each cross section. The reason is that the frames corresponding to the rapid-filling phase are included when the number of frames N is larger and the heart wall moves and deforms rapidly in the rapid-filling phase. Therefore, a smaller number of frames N was optimum in the slow-filling phase.

As described above, in the long-axis view, the optimum cardiac phase is the early slow-filling phase and the optimal number of frames N is 70. In the short-axis view, the optimum cardiac phase is the early atrial systole and the optimal number of frames N is 150. Table I summarizes the optimal cardiac phase and the number of frames N in each view.

3.2 Optimization of MTI filtering

Echoes from the heart wall are likely to be affected by MTI filtering because the motion of the heart wall is smaller than those of blood particles. The suppression of the echo signal from the heart wall possibly degrades separability because the echogenicity and MSC in the heart wall become also lower. Thus, in the present study, MTI filtering was applied to the region with a limited depth, which includes most of the clutter echoes, to preserve the echo signal from the heart wall. Figure 10(b) shows the power spectrum at each depth

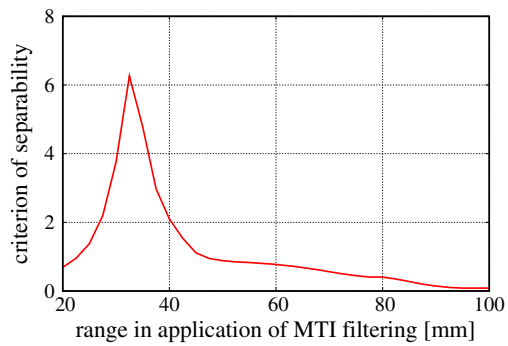

Fig. 11. (Color online) Separability plotted as a function of range applied with MTI filtering.

obtained by applying DFT with respect to the frame [window size: 50 frames (= 0.09 s)] to RF echoes from manually assigned regions of RV, IVS, and LV shown in Fig. 10(a) at the best frame for classification. The power spectra were averaged for all scan lines. As shown in Fig. 10(b), the components with low velocity and high magnitude could be clutter echoes, and the clutter component becomes lower as the position becomes deeper. The optimal cut-off frequency is determined to be 50 Hz because the clutter components exist under approximately 50 Hz. Although echo signals in IVS should include echoes from the heart wall (IVS) and clutter echoes, it is difficult to distinguish between them, as shown in Fig. 10(b). Therefore, the range (depth), to which the MTI filter was applied, was changed from 20 to 100 mm, and the criterion of separability J was evaluated. Figure 11 shows the criterion of separability J plotted as a function of the range for MTI filtering. The result shows that the range of 33 mm was the optimum range for MTI filtering. Figures 12(a), 12(b), and 12(c) show the spatial distributions of MSC without the MTI filter, MSC with MTI filtering (cut-off frequency: 10 Hz),[21] and MSC with MTI filtering applied to the limited range, respectively. Using the previsously determined MTI filtering [Fig. 12(b)], MSCs lower than those without MTI filtering in the heart wall are found and the clutter components are not sufficiently suppressed, as shown in Fig. 12(b). On the other hand, MTI filtering applied to the limited range resulted in the reduction of clutter components in the right ventricle while preserving MSC in the heart wall, as shown Fig. 12(c).

3.3 Effect of AM filtering and segmentation of in vivo ultrasonic data

Figures 13 and 14 show MSCs obtained from the long-axis and short-axis views, respectively. In Figs. 13 and 14, original MSC images (a) and AM-filtered MSC images (b) are shown. Particularly in the short-axis view, spotlike regions with low MSCs are observed in the lateral wall, as shown in Fig. 14(a). By AM filtering, such regions were eliminated because of smoothing of MSC using the information of surrounding points. By applying AM filtering, the criterion of separability J improved from 11.3 to 15.7 for the data of the long-axis view and from 9.0 to 12.5 for the short-axis view.

Figures 15 and 16 show the results of classifications in the long-axis and short-axis views, respectively: (a) B-mode images, (b) results of the identification of the heart wall

© 2014 The Japan Society of Applied Physics

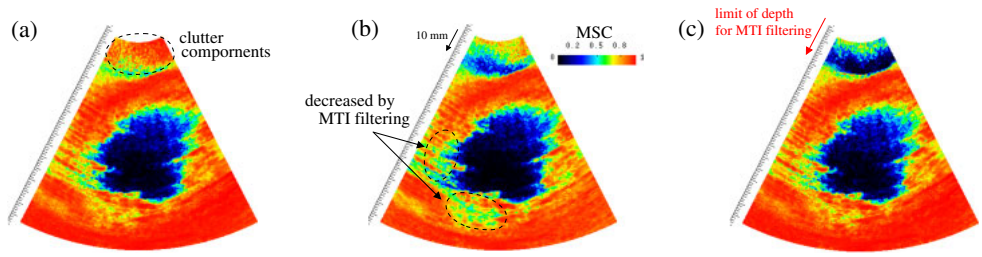

Fig. 12. (Color online) Spatial distribution of MSC applied by MTI filtering limited in depth: (a) MSC image without MTI filter. (b) MSC image with previously determined filtering (cut-off frequency: 10 Hz).[21] (c) MSC image with MTI filtering applied to limited range.

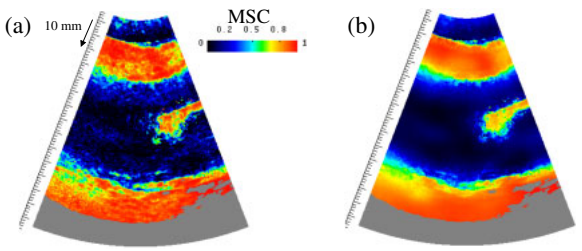

Fig. 13. (Color online) Result of applying AM filtering to MSC obtained in long-axis view of left ventricle: (a) Original MSC image. (b) Filtered MSC image.

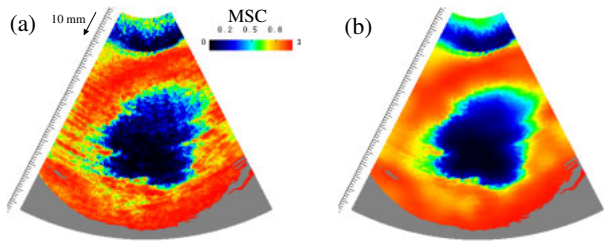

Fig. 14. (Color online) Result of applying AM filtering to MSC obtained in short-axis view of left ventricle: (a) Original MSC image. (b) Filtered MSC image.

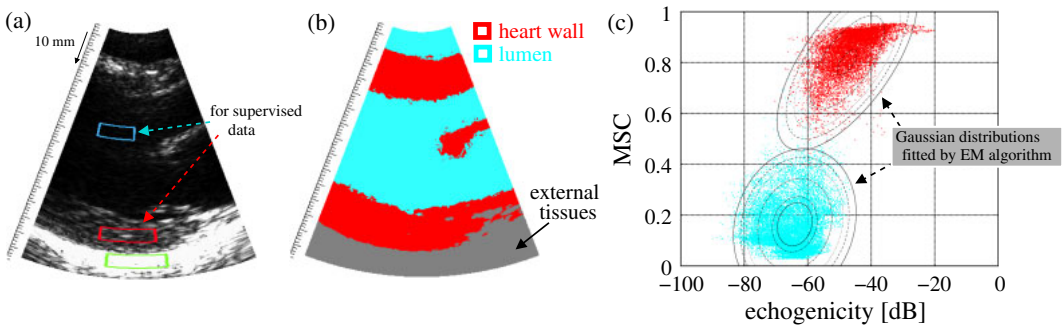

Fig. 15. (Color online) Result of segmentation in long-axis view of left ventricle: (a) B-mode image. (b) Result of identification of the heart wall regions. (c) Distribution of features of region manually assigned as each tissue in 2D feature space and Gaussian distribution fitted into features of each distribution.

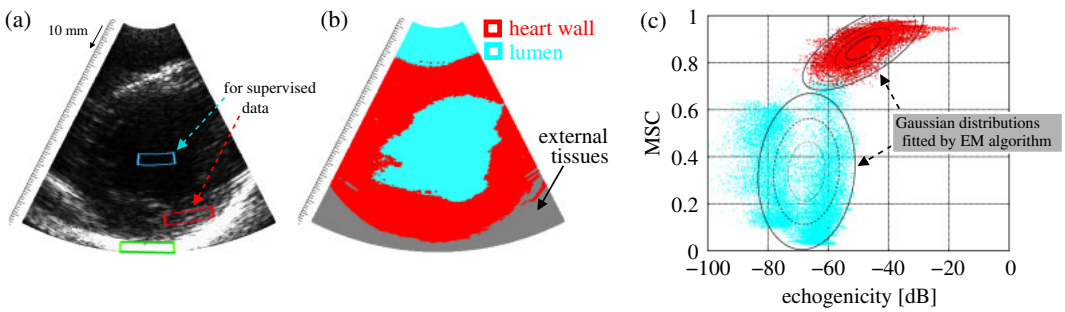

Fig. 16. (Color online) Result of segmentation in short-axis view of left ventricle: (a) B-mode image. (b) Result of identification of the heart wall regions. (c) Distribution of features of region manually assigned as each tissue in 2D feature space and Gaussian distribution fitted into features of each distribution.

regions in the optimal cardiac phase with the optimum number of frames N, and (c) feature distributions of the heart wall and lumen extracted from manually assigned regions with the corresponding Gaussian distributions estimated using the EM algorithm.[24] The red regions in Figs. 15(b) and 16(b) are the regions identified as the heart wall, and the results show that accurate segmentation was possible in both long-axis and short-axis views by the proposed method. As can also be seen in Figs. 15(c) and 16(c), the features extracted under the optimal condition show high separabilities.

© 2014 The Japan Society of Applied Physics

4. Conclusion

The aim of the present study was the identification of the heart wall in ultrasound data obtained in various cross sections. In the present study, we have shown that an accurate segmentation can also be realized in the short-axis view by optimizing the optimum cardiac phase and number of frames for the calculation of MSC. Moreover, AM filtering was effective, particularly in the short-axis view, in elimination of spotlike regions with low MSCs. Furthermore, the MTI filtering applied to a limited range resulted in the reduction of clutter components in the right ventricle while preserving MSC in the heart wall. Through these optimizations, it was shown that accurate segmentation was possible in both long-axis and short-axis views by the proposed method.

1) G. R. Sutherland, G. D. Salvo, P. Claus, J. D'hooge, and B. Bijnens, J. Am. Soc. Echocardiogr. **17**, 788 (2004).
2) W. N. McDicken, G. R. Sutherland, C. M. Moran, and L. N. Gordon, Ultrasound Med. Biol. **18**, 651 (1992).
3) L. N. Bohs, B. J. Geinman, M. E. Anderson, S. C. Gebhart, and G. E. Trahey, Ultrasonics **38**, 369 (2000).
4) K. Kaluzynski, X. Chen, S. Y. Emelianov, A. R. Skovoroda, and M. O'Donnell, IEEE Trans. Ultrason. Ferroelectr. Freq. Control **48**, 1111 (2001).
5) J. D'hooge, E. Konofagou, F. Jamal, A. Heimdal, L. Barrios, B. Bijnens, J. Theoen, F. V. der Werf, G. R. Sutherland, and P. Suetens, IEEE Trans. Ultrason. Ferroelectr. Freq. Control **49**, 281 (2002).
6) Y. Honjo, H. Hasegawa, and H. Kanai, Jpn. J. Appl. Phys. **49**, 07HF14 (2010).
7) Y. Honjo, H. Hasegawa, and H. Kanai, Jpn. J. Appl. Phys. **51**, 07GF06 (2012).
8) H. Kanai, IEEE Trans. Ultrason. Ferroelectr. Freq. Control **52**, 1931 (2005).
9) H. Yoshiara, H. Hasegawa, H. Kanai, and M. Tanaka, Jpn. J. Appl. Phys. **46**, 4889 (2007).
10) H. Kanai, Ultrasound Med. Biol. **35**, 936 (2009).
11) H. Shida, H. Hasegawa, and H. Kanai, Jpn. J. Appl. Phys. **51**, 07GF05 (2012).
12) V. Chalana and Y. Kim, IEEE Trans. Med. Imaging **16**, 642 (1997).
13) E. Brandt, L. Wigström, and B. Wranne, Proc. MICCI'99, 1999, p. 410.
14) Q. Duan, E. D. Angelini, S. L. Herz, C. M. Ingrassia, K. D. Costa, J. W. Holmes, S. Homma, and A. F. Laine, Ultrasound Med. Biol. **35**, 256 (2009).
15) N. Ibrahim, H. Hasegawa, and H. Kanai, Jpn. J. Appl. Phys. **51**, 07GF07 (2012).
16) N. Ibrahim, H. Hasegawa, and H. Kanai, Jpn. J. Appl. Phys. **52**, 07HF03 (2013).
17) C. Y. Chang, Y. F. Lei, C. H. Tseng, and S. R. Shih, IEEE Trans. Med. Imaging **57**, 1348 (2010).
18) A. H. Torp, S. I. Rabben, A. Støylen, H. Ihlen, K. Anderson, L. Å. Brodin, and B. Olstad, Proc. IEEE Ultrasonics Symp., 2004, p. 474.
19) M. M. Nillesen, R. G. P. Lopata, I. H. Gerrits, L. Kapusta, H. J. Huisman, J. M. Thussen, and C. L. D. Korte, Ultrasound Med. Biol. **33**, 1453 (2007).
20) T. Kinugawa, H. Hasegawa, and H. Kanai, Jpn. J. Appl. Phys. **47**, 4155 (2008).
21) H. Takahashi, H. Hasegawa, and H. Kanai, Jpn. J. Appl. Phys. **50**, 07HF16 (2011).
22) H. Takahashi, H. Hasegawa, and H. Kanai, Jpn. J. Appl. Phys. **52**, 07HF17 (2013).
23) M. R. Holland, U. M. Wilkenshoff, A. E. Finch-Johnston, S. M. Handley, J. E. Perez, and J. G. Miller, J. Am. Soc. Echocardiogr. **11**, 929 (1998).
24) C. M. Bishop, *Pattern Recognition and Machine Learning* (Springer, Berlin, 2006).
25) B. Hete and K. K. Shung, IEEE Trans. Ultrason. Ferroelectr. Freq. Control **40**, 354 (1993).
26) S. A. Wickline, L. J. Thomas, II, J. G. Miller, B. E. Sobel, and J. E. Perez, J. Clin. Invest. **76**, 2151 (1985).
27) H. Kanai, M. Sato, Y. Koiwa, and N. Chubachi, IEEE Trans. Ultrason. Ferroelectr. Freq. Control **43**, 791 (1996).
28) H. Takahashi, H. Hasegawa, and H. Kanai, Cho-onpa Igaku **36**, 679 (2009) [in Japanese].
29) T. Higuchi and M. Kawamata, *Dijitaru Singoshori: MATLAB Taio* (Digital Signal Processing: With MATLAB Exercises) (Shokado, Tokyo, 2000) [in Japanese].
30) B. R. Mahafza, *Introduction to Radar Analysis* (CRC Press, Boca Raton, FL, 1998).
31) M. Tanter, J. Bercoff, L. Sandrin, and M. Fink, IEEE Trans. Ultrason. Ferroelectr. Freq. Control **49**, 1363 (2002).
32) H. Hasegawa and H. Kanai, IEEE Trans. Ultrason. Ferroelectr. Freq. Control **55**, 2626 (2008).
33) K. Fukunaga, *Introduction to Statistical Pattern Recognition* (Academic Press, Boston, MA, 1990) 2nd ed.

© 2014 The Japan Society of Applied Physics